

SUPPORTING INFORMATION SECTION

Fe and Mn oxidation states by TEM-EELS in fine-particle emissions from a Fe-Mn alloy making plant

Hélène Marris^a, Karine Deboudt^{a,*}, Pascal Flament^a, Bernard Grobéty^b, Reto Gieré^c.

^a Université du Littoral Côte d'Opale, Laboratoire de Physico-Chimie de l'Atmosphère (LPCA), Bâtiment MREI2, 189A avenue Maurice Schumann, 59140 Dunkerque, France

^b Department of Geosciences, University of Fribourg, Ch. du Musée 6, CH-1700 Fribourg, Switzerland

^c Institut für Geo- und Umweltwissenschaften, Albert-Ludwigs-Universität, Albertrasse 23b, D-79104 Freiburg, Germany

* Corresponding author: Tel.: +33/328237631; Fax.: +33/328658244; email address: karine.deboudt@univ-littoral.fr

MATERIALS AND METHODS

Fe and Mn oxidation-state determination by TEM-EELS. Energy-loss edge structures of *L* ionization edges of transition metals with partially filled *3d* orbitals show characteristic white lines due to transitions of excited *2p* electrons into unoccupied *d*-orbitals [1]. In order to correlate the observed signals with the oxidation states, EEL spectra from mineral and synthetic standards were acquired. They were prepared by grinding crushed material suspended in 100% cyclohexane in an agate mortar with a pestle. The suspension was withdrawn using a micropipette and dropped onto a holey-carbon TEM grid. Commercially

available minerals and synthetic Fe and Mn oxides were used as calibration standards (Table S1). The identity of the standards was confirmed by powder X-ray diffractometry.

The Fe oxidation state can be measured either by a calibrated relationship between Fe- L_3 and $-L_2$ white-line intensity ratios in EEL spectra [2] (method 1) or by fitting Gaussian line profiles to the Fe- L_3 edge, where the ratio of $\text{Fe}^{3+}/\sum\text{Fe}$ is determined from the areas under the fitted peaks [3, 4] (method 2). This method, developed by Garvie and Buseck (1998) and especially adapted for Fe oxides, employs the premise that spectra from mixed-valence minerals are simple linear combinations of two valence end-member compositions [5]. The Mn oxidation state can be estimated by 1) a calibrated relationship between either Mn- L_3 and $-L_2$ white-line intensity ratios in EEL spectra (L_3/L_2 white-line intensity ratio increases with decreasing oxidation state) or Mn- L_3 and $-L_2$ energy-peak separation (i.e., the energy difference between the L_3 and L_2 peaks increases with decreasing valence), or by 2) recording the energy-loss position of the Mn- L edge, a feature identified as the chemical shift (chemical shift increases with oxidation state). The energy of the beam is prone to drift in TEM-EELS, which results in random fluctuations of the signal along the energy-loss scale [6]. An internal standard needs to be used to provide a means of calibrating the absolute energy loss of the Mn- L edge [7]. However, we were unable to use an internal standard in our case, and thus, the Mn oxidation state was estimated from the calculated L_3/L_2 white-line intensity ratios. Moreover, the ratio of the white-line intensities is likely to be a reliable and sensitive approach. The calculated L_3/L_2 is rather stable and is not dependent on specimen thickness [1, 7-11].

RESULTS

Iron Calibration. Fe oxidation state measurements were calibrated using iron oxide mineral standards of known oxidation state (Table S1). The purity of these standards was confirmed

by XRD. Magnetite was analyzed as unknown by TEM-EELS to verify that the methods produced reliable results for samples of known iron valence. Ten particles of each standard were analyzed, and their purity was confirmed by EDX.

The EEL spectra obtained from the hematite and fayalite standards were compiled after background subtraction to produce a calibration curve, which was used to calculate $\text{Fe}^{3+}/\sum\text{Fe}$ values for unknowns (method 1). In parallel, one spectrum of each standard was chosen regarding $L_{2,3}$ white-line characteristics as end-members for the fitting method (method 2), with the peak maximum for Fe(II) and Fe(III) occurring at 707.5 and 709.5 eV, respectively (Figure S1). The end-member spectra were then scaled to each other by normalizing the data to the area under the continuum well above the $L_{2,3}$ white lines. The unknown mixed-valence spectra were calibrated with the peak maximum at 708.5 eV and were then simulated by a multiple, linear, least-square fitting method with the 2 end-member spectra. This fitting method permits a slight shift of the energy scale of the unknown compound (± 1.5 eV), which does not require proper energy calibration.

Magnetite analyses (Table S2) scatter from 46.2 to 111.6% for method 1 and from 47.5 to 67.1 for method 2 including the anticipated ratio (66.6) with a precision of $\pm 33\%$ for method 1 and $\pm 10\%$ for method 2. Contrary to method 1, which requires sufficient intensity of the Fe- $L_{2,3}$ edge, the fitting method (method 2) is more reliable and yields an error in the range of $\leq 10\%$ on $\text{Fe}^{3+}/\sum\text{Fe}$ for samples with contents of $> 2\%$ atomic Fe [4, 5]. Iron oxidation states were thus estimated in the studied industrial particles by the fitting method, since iron concentrations are relatively low ($< 5\%$ at.) in all collected particulate samples (Table S3). In the manuscript, results for iron oxidation state are discussed with the nominal values rather than the $\text{Fe}^{3+}/\sum\text{Fe}$ ratios.

Manganese Calibration. Since the L_3/L_2 intensity ratio is directly related to the oxidation state of the corresponding element, a series of 10 EEL spectra was acquired from each of several standard specimens with known oxidation states (Table S1). An empirical plot of these data served as reference for determining the oxidation state of the element present in an unknown compound. The best fit was a polynomial of the general form $y=ax^3+bx^2+cx+d$, where x is the L_3/L_2 intensity ratio (Figure S2) and y is the oxidation state. Moreover, the $L_{2,3}$ -edge shapes obtained from the Mn oxide standards are dependent on the oxidation states, and the energy difference between the L_3 and L_2 peaks increases with decreasing in oxidation state (Figure S3), which is consistent with literature data [1, 7, 10].

Influence of beam damage on oxidation state. Electron irradiation is known to damage various oxides compounds [12]. In order to evaluate beam damage on iron and manganese oxidation state, 5 spectra were acquired successively for selected particles collected from the industrial emissions. Figure S4 clearly reveals the gradual alteration of the Mn and Fe oxidation state, probably depending on the size and chemical composition. However, the changes are relatively minor for the first three spectra. Based on these results, the following precautions were taken in order to prevent beam-damage effects on oxidation state: The electron beam was not fully focused all the time; the sample was checked before and after analysis for signs of beam damage (imaging); and the acquisition time was kept to a minimum.

REFERENCES

1. Schmid, H. K.; Mader, W., Oxidation states of Mn and Fe in various compound oxide systems. *Micron* **2006**, *37*, 426-432.

2. Cavé, L.; Al, T.; Loomer, D.; Cogswell, S.; Weaver, L., A STEM/EELS method for mapping iron valence ratios in oxide minerals. *Micron* **2006**, *37*, (4), 301-309.
3. Van Aken, P. A.; Liebscher, B., Quantification of ferrous/ferric ratios in minerals: New evaluation schemes of Fe $L_{2,3}$ electron energy-loss near-edge spectra. *Phys. Chem. Minerals* **2002**, *29*, 188-200.
4. Calvert, C. C.; Brown, A.; Brydson, R., Determination of the local chemistry of iron in inorganic and organic materials. *Journal of Electron Spectroscopy and Related Phenomena* **2005**, *143*, (2-3), 173-187.
5. Garvie, L.; Buseck, P., Ratios of ferrous to ferric iron from nanometre-sized areas in minerals. *Nature* **1998**, *396*, (6712), 667-670.
6. Potapov, P. L.; Schryvers, D., Measuring the absolute position of EELS ionisation edges in a TEM. *Ultramicroscopy* **2004**, *99*, 73-85.
7. Loomer, D.; Al, T.; Weaver, L.; Cogswell, S., Manganese valence imaging in Mn minerals at the nanoscale using STEM-EELS. *American Mineralogist* **2007**, *92*, 72-79.
8. Estrade, S.; Yedra, L.; Lopez-Ortega, A.; Estrader, M.; Salazar-Alvarez, G.; Baro, M.; Nogues, J.; Peiro, F., Distinguishing the core from the shell in MnOx/MnOy and FeOx/MnOx core/shell nanoparticles through quantitative electron energy loss spectroscopy (EELS) analysis. *Micron* **2011**, doi:10.1016/j.micron.2011.04.002.
9. Wang, Z. L.; Bentley, J.; Evans, N. D., Valence state mapping of cobalt and manganese using near-edge fine structures. *Micron* **2000**, *31*, (4), 355-362.
10. Wang, Z. L.; Yin, J. S.; Jiang, Y. D., EELS analysis of cation valence states and oxygen vacancies in magnetic oxides. *Micron* **2000**, *31*, 571-580.
11. Zhang, S.; Livi, K.; Gaillot, A. C.; Stone, A.; Veblen, D., Determination of manganese valence states in (Mn³⁺, Mn⁴⁺) minerals by electron energy loss-spectroscopy. *American Mineralogist* **2010**, *95*, 1741-1746.

12. Davoisne, C.; Leroux, H., Structural and compositional modifications of fayalite Fe_2SiO_4 under electron irradiation. *Nuclear Instruments and Methods in Physics Research B* **2006**, *243*, 371-376.

Table S1: Synthetic Mn-oxide and Fe-mineral standards used for acquisition of EEL spectra.

Mineral	Chemical formula	Mn nominal valence
Pyrolusite	MnO ₂	+ IV
Bixbyite	Mn ₂ O ₃	+ III
Hausmannite	Mn ₃ O ₄	+ II, + III (2.67)
Manganosite	MnO	+ II

Mineral	Chemical formula	Fe nominal valence
Hematite	Fe ₂ O ₃	+ III
Magnetite	Fe ₃ O ₄	+ II, + III (2.67)
Fayalite	Fe ₂ SiO ₄	+ II

Table S2: Measured $\text{Fe}^{3+}/\Sigma\text{Fe}$ ratios (in %) for mineral standard (magnetite) as determined with the calibration curve (method 1) and with the fitting method (method 2): mean value \pm one standard deviation for 10 analyzed particles.

	Magnetite
$\text{Fe}^{3+}/\Sigma\text{Fe}$ nominal	66.6 ± 0.1
$\text{Fe}^{3+}/\Sigma\text{Fe}$ (method 1)	78.9 ± 32.7
$\text{Fe}^{3+}/\Sigma\text{Fe}$ (method 2)	57.3 ± 9.8

Table S3: Elemental composition of source particles collected inside chimney B (CB).

Type of particles	Size fraction	Relative abundance	Average chemical composition* (atomic %)
Aluminosilicate	PM _{0.1-1}	18%	C(1.0) O(57.0) Al(17.6) Si(16.8) K(1.8) Mn(2.1) Fe(1.3)
	PM ₁₋₁₀	20%	C(1.7) O(55.7) Al(17.3) Si(16.4) K(2.5) Mn(1.7)
Metallic	PM _{0.1-1}	17%	C(1.2) O(60.7) Al(3.2) Si(1.5) S(1.1) K(1.7) Mn(24.2) Fe(3.3)
	PM ₁₋₁₀	32%	C(2.5) O(58.2) Mg(1.2) Al(3.3) Si(2.4) K(2.5) Mn(23.1) Fe(3.6)
Mixed Aluminosilicate-Metallic	PM _{0.1-1}	60%	C(1.1) O(58.1) Al(9.3) Si(4.9) K(1.4) Mn(17.6) Fe(4.1)
	PM ₁₋₁₀	44%	C(1.8) O(55.4) Mg(1.3) Al(9.5) Si(5.7) K(2.9) Mn(15.8) Fe(3.9)
Other	PM _{0.1-1}	5%	This class contains all particle types not classified above.
	PM ₁₋₁₀	4%	

*Major elements are in bold. Elements with mean concentrations < 1 atomic % are not reported

Table S4: Average elemental composition of clusters obtained by Hierarchical Ascendant Classification of automated SEM-EDX data for metallic source particles. Due to the paucity of particles, no data are available for samples “Chimney A, PM_{0.1-1}” and “Chimney C, PM₁₋₁₀”.

Sample	Number of particles	Cluster	Relative abundance	Average elemental concentration (atomic %)
Chimney A PM ₁₋₁₀	40	1	28%	O(60) Fe(23)
		2	62%	O(62) Mn(24)
		3	10%	C(12) O(41) K(10) Mn (5) Fe(6)
Chimney B PM _{0.1-1}	78	1	12%	C(9) O(49) K(6) Mn(19)
		2	76%	O(59) Mn(26)
		3	9%	O(60) Mn(12) Fe(10)
		4	3%	O(65) Fe(26)
Chimney B PM ₁₋₁₀	147	1	89%	O(62) Mn(26)
		2	6%	C(6) O(52) S(10) K(10) Mn(10)
		3	5%	O(61) Mn(5) Fe(25)
Chimney C PM _{0.1-1}	421	1	75%	O(63) Fe(25)
		2	8%	C(8) N(5) O(60) Fe(20)
		3	4%	O(55) Mn(29)
		4	6%	O(59) S(8) Mn(10) Fe(6)
		5	7%	O(66) S(7) Fe(16)

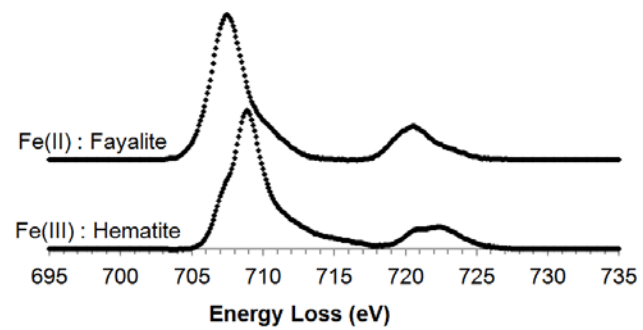


Figure S1: EEL spectra of hematite and fayalite standards displaying different Fe- $L_{2,3}$ white-line characteristics.

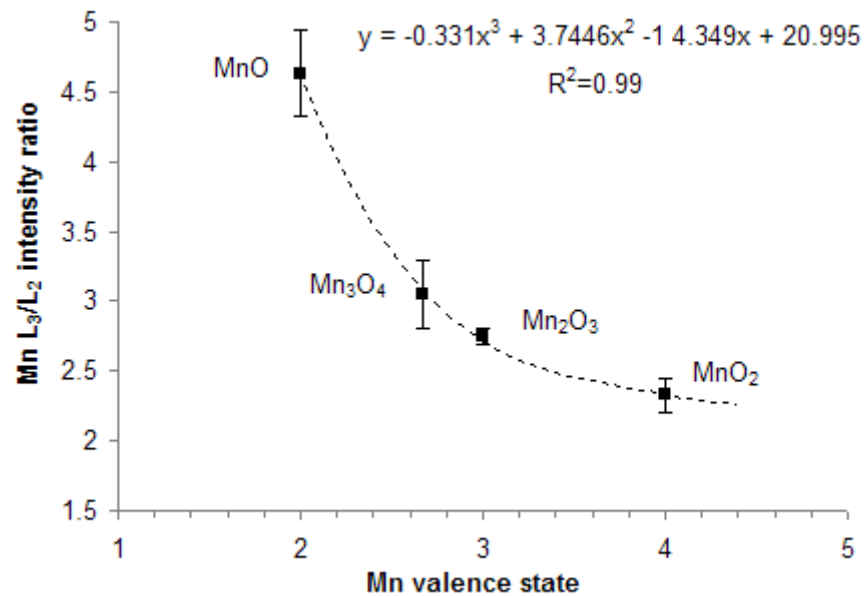


Figure S2: Calibration curve of L₃/L₂ intensity ratio, as calculated from EEL spectra acquired for synthetic Mn-oxide standards, as a function of the cation oxidation state. The dashed curve shows nominal fit of the experimental data.

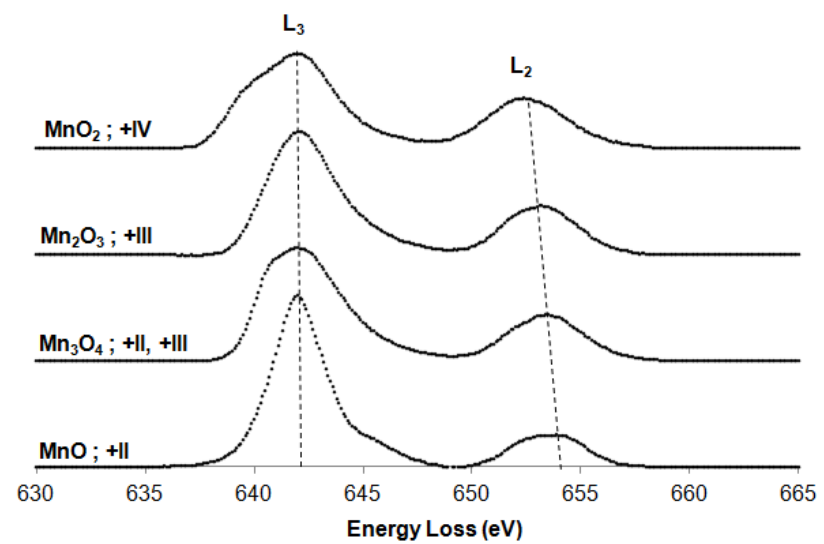


Figure S3: Comparison of EEL spectra of the synthetic Mn-oxide standards, which display different Mn-L_{2,3} white-line characteristics. The distance between the Mn-L₃ and -L₂ energy peaks increases with decreasing oxidation state.

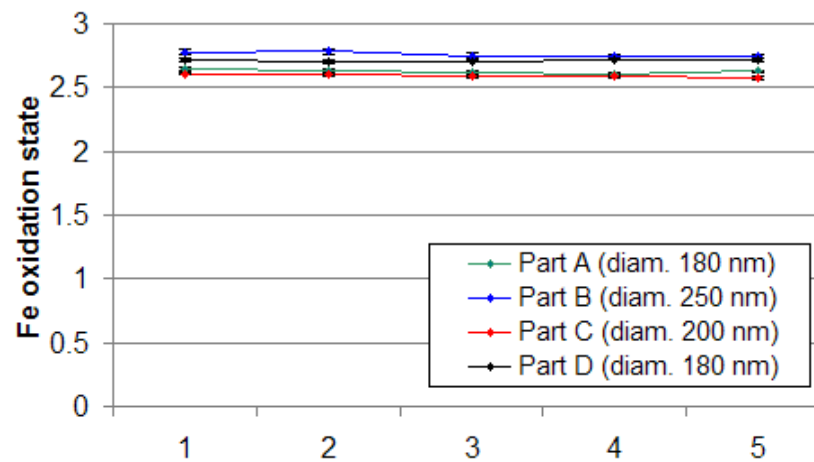
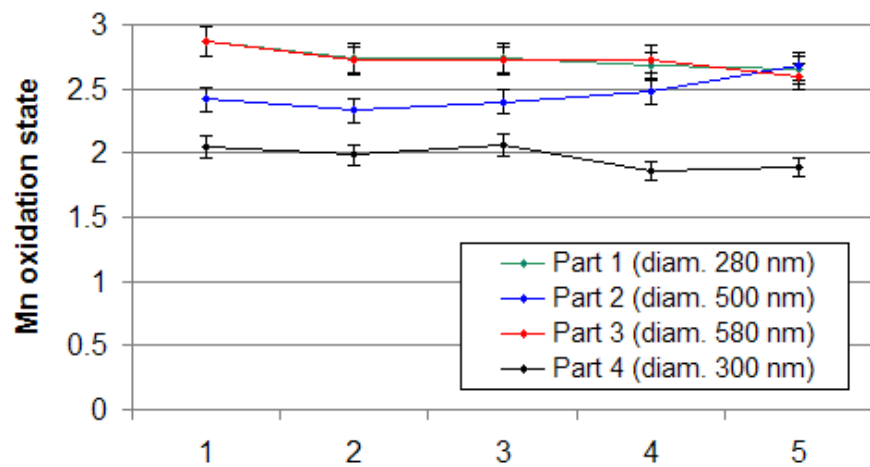


Figure S4: Evolution of Mn (left) and Fe (right) oxidation states in industrial particles under electron irradiation, during acquisition of five consecutive spectra (1 → 5).